14th International Symposium on Turbulence and Shear Flow Phenomena (TSFP14)
Heidelberg, Germany, July 28–31, 2026

DATA-DRIVEN UPSAMPLING REVEALS AMPLITUDE MODULATION IN THE TURBULENT SEPARATED WAKE OF A 3D GAUSSIAN BUMP

Kevin H. Manohar[1], **Chris Morton**[2], **Robert J. Martinuzzi**[3], **and Owen Williams**[1†]
[1] Department of Aeronautics and Astronautics, University of Washington, Seattle, WA, USA
[2] Department of Mechanical Engineering, McMaster University, Hamilton, ON, Canada
[3] Department of Mechanical and Manufacturing Engineering, University of Calgary, Calgary, AB, Canada
[1]kmanoh@uw.edu, [2]mortoc5@mcmaster.ca, [3]rmartinu@ucalgary.ca, [1†]ojhw@uw.edu

ABSTRACT

Understanding the nonlinear interactions between unsteady modes with disparate timescales remains a central challenge in turbulent flow analysis. In the turbulent separated wake over the Boeing Gaussian bump, a very-low-frequency (VLF) spanwise spatially antisymmetric meandering mode coexists with faster spatially symmetric motions, including low-frequency (LF) breathing and high-frequency (HF) shedding modes. Previous symmetry/antisymmetry proper orthogonal decomposition (POD) analyses revealed distinct parabolic envelopes in joint histograms of the leading antisymmetric and symmetric modal coefficients, suggesting amplitude-dependent coupling between these motions. We demonstrate that these parabolic structures arise from the amplitude modulation of the symmetric motions by the VLF meander. As the available 15 Hz PIV is insufficient to extract the required analytic envelopes, we train a temporal Transformer on synchronized high-speed wall-pressure data to upsample the PIV coefficients to $\sim$1.2 kHz. Coefficient-based spectral POD and Hilbert demodulation show that the observed structure is primarily associated with the LF breathing band. As the VLF amplitude increases, the LF breathing envelope strengthens while the HF shedding envelope weakens. These responses are also strongly phase-dependent, with the greatest LF amplification and HF suppression occurring near phases of maximum spanwise wake deflection.

1 INTRODUCTION & MOTIVATION

In a streamwise-spanwise plane of the turbulent separated wake over the 3D Gaussian bump (Williams *et al.*, 2020), synchronized PIV and wall-pressure measurements have revealed three energetic families of motion in the separated region (Manohar *et al.*, 2026): (i) a very-low-frequency (VLF) spanwise antisymmetric meandering mode centered near $St_{L_{\mathrm{sep}}} = fL_{\mathrm{sep}}/U_\infty = 0.005$ where L_{sep} is the mean separation length (1 Hz or $St_H \sim 10^{-3}$ based on bump height H), corresponding to a slow lateral displacement of the separated wake about the centreline, (ii) a broadband low-frequency (LF) "breathing" motion associated with expansion and contraction of the separated region, centered near $St_{L_{\mathrm{sep}}} \approx 0.068$ (13.5 Hz), and (iii) a broadband higher-frequency (HF) vortex-shedding mode associated with oscillatory shear-layer roll-up near the centreline, centered near $St_{L_{\mathrm{sep}}} \approx 0.68$ (135 Hz).

A convenient way to isolate these motions is through a symmetry/antisymmetry (S/A) POD with respect to the geometric centreline y=0. This decomposition was recently used by Manohar *et al.* (2026), to separate the wake into antisymmetric and symmetric coefficients, $a^{(n)}(t)$ and $s^{(n)}(t)$, respectively, with the leading antisymmetric coefficient $a^{(1)}$ associated with the VLF meandering mode. The resulting two-dimensional (2D) joint histograms between $a^{(1)}$ and the leading symmetric coefficients (e.g., $s^{(1)}$) display distinct parabolic envelopes, as shown in Fig. 1d,e.

Such parabolic dependencies are a recurring feature of modal interactions in separated flows. In classic 2D wakes, the amplitudes of the antisymmetric vortex shedding modes induce a quadratic mean-flow deformation, often represented by a symmetric "shift mode" that constrains the dynamics along a parabolic manifold in modal space (Noack *et al.*, 2003). Similar parabolic S/A couplings have since been observed in 3D bluff-body wakes, where the strength of a fast antisymmetric vortex shedding mode depends on the instantaneous state of a slower symmetric drift mode, producing approximately parabolic phase portraits between the corresponding modal coefficients (Da Silva *et al.*, 2024). In the present bump flow, however, the roles appear reversed: the dominant slow mode is antisymmetric, while the faster breathing and shedding motions reside primarily in the symmetric subspace. This suggests that the observed parabolic envelopes may reflect a slow antisymmetric meander that modulates the instantaneous energy of the faster symmetric dynamics through an analogous quadratic coupling mechanism. The present work seeks to determine how these parabolic envelopes relate to the underlying LF breathing and HF shedding dynamics, and whether the VLF meander similarly modulates the instantaneous energy of these faster symmetric motions.

1.1 Symmetry Argument for the Parabolic Envelope

We now show that the reflection symmetry of the wake, together with the timescale separation between the antisymmetric VLF and symmetric LF/HF motions, motivates the expectation of a quadratic or parabolic relationship between $a^{(1)}$ and the symmetric coefficients. Expanding the velocity fluctuations $\mathbf{u}'(\mathbf{x},t)$ using the S/A POD basis yields:

$$\mathbf{u}'(\mathbf{x},t) = a^{(1)}(t)\mathbf{\Phi}_A(\mathbf{x}) + \sum_n s^{(n)}(t)\mathbf{\Phi}_{S,n}(\mathbf{x}), \qquad (1)$$

where $\mathbf{\Phi}_A \in \mathbb{R}^M$ represents the dominant antisymmetric VLF meander and $\mathbf{\Phi}_{S,n} \in \mathbb{R}^M$ represent the symmetric motions (e.g., breathing and shedding), where M is the number of spatial degrees of freedom. Since the governing equations and

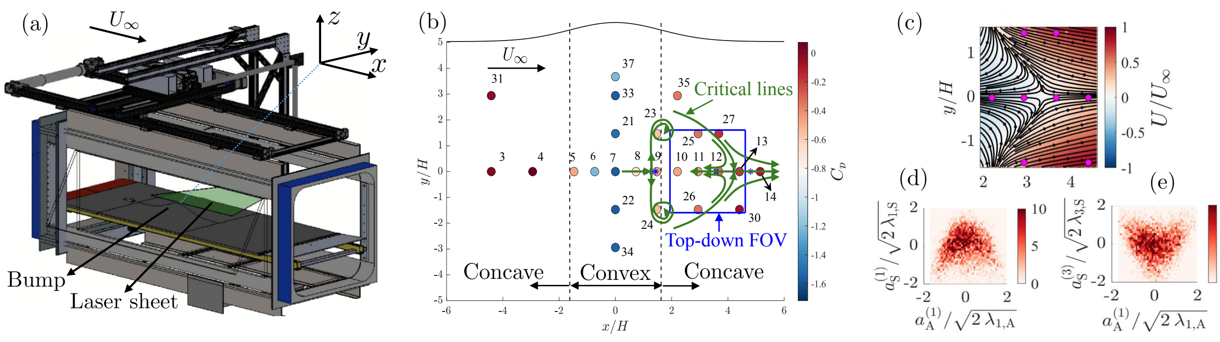

Figure 1. (a) PIV setup to acquire streamwise-spanwise field-of-view (top-down). (b) Wall–pressure tap array relative to top–down PIV field-of-view with side-on bump profile on top. (c) Mean velocity field with select pressure taps projected. (d,e) Bivariate histograms from 15 Hz PIV showing parabolic envelopes in $(a^{(1)}, s^{(1)})$ and $(a^{(1)}, s^{(3)})$. Axes (x, y) centered on top of bump.

mean wake are approximately invariant under spanwise reflection (Fig. 1c), the nonlinear mode couplings must preserve symmetry (Holmes, 2012). In particular, the quadratic self-interaction of an antisymmetric mode produces a symmetric contribution. As shown in Appendix A.1, a Galerkin projection onto the symmetric modes yields, at leading order, a reduced-order dynamical system in which the lowest-order forcing from the antisymmetric meander into the symmetric dynamics is even, with the minimal contribution proportional to $[a^{(1)}]^2$.

To observe this coupling in experimental data, we must account for the distinct temporal dynamics of the modes. The separated wake exhibits a strong hierarchy of timescales, with VLF meandering ($\sim$1 Hz) much slower than the LF breathing ($\sim$13.5 Hz) and HF shedding ($\sim$135 Hz) (Manohar *et al.*, 2026). This timescale separation naturally maps onto the signal-processing concepts of a slow modulating "driver" and faster "carrier" oscillations. Here, the VLF meander acts as the driver, while the LF breathing and HF shedding motions act as carriers whose amplitudes vary with the instantaneous meandering of the wake state. Since the carrier motions oscillate rapidly about zero mean, their interaction with the slowly evolving $[a^{(1)}]^2$ forcing is expected to appear most clearly in their amplitude envelopes rather than in the raw waveforms themselves. While this quadratic forcing is expressed in terms of $a^{(1)}(t)$, this corresponds to a dependence on its squared amplitude. This motivates the use of Hilbert-based envelope extraction to determine whether the LF and HF motions strengthen or weaken with increasing VLF amplitude.

We therefore hypothesize that the conditional mean envelope of the symmetric bands scales with the square of the meander amplitude. Such behavior would be consistent with the leading-order coupling predicted by the Galerkin argument and would provide evidence that the slow meander modulates the instantaneous amplitude of the faster symmetric motions.

1.2 Objectives

Diagnosing this amplitude modulation (AM) mechanism requires time-resolved sequences from which analytic (Hilbert) envelopes can be extracted. However, the available PIV (15 Hz) only marginally resolves the 1 Hz meandering motion and aliases the LF and HF bands. The objective of the present work is therefore to overcome this limitation through data-driven upsampling, enabling us to:

- Determine whether the observed parabola is associated with amplitude-envelope modulation of the symmetric motions, and
- Identify whether the LF breathing band, the HF shedding band, or both contribute to the observed parabola.

To realize these objectives, we employ a hybrid experimental and data-driven methodology. Synchronized low-speed PIV and time-resolved wall-pressure measurements acquired by Manohar *et al.* (2026) are used to characterize the baseline wake dynamics. These datasets are then used to train a temporal-Transformer, an attention-based neural network (Vaswani *et al.*, 2017), yielding the time-resolved modal coefficients required for the envelope diagnostics.

2 METHODS

2.1 Geometry and Datasets

Experiments were performed in the University of Washington 3×3 Low-Speed wind tunnel using top–down (streamwise-spanwise plane) planar PIV at 15 Hz (see Fig. 1a for setup) and 14 synchronized wall-pressure taps (centreline taps 7–8 and 11–14, together with off-centreline taps 21–27 and 30; see Fig. 1b) sampled at 31.25 kHz. The total number of PIV snapshots recorded was $N = 2660$, spanning about 177 seconds. Fig. 1b shows the wall-pressure tap layout relative to both the top–down PIV field-of-view located at z/H=0.53 above the surface of the splitter plate as well as the approximate projected critical lines inferred from surface-flow visualization (Williams *et al.*, 2020). The mean PIV field is shown in Fig. 1c. Additional details on the experimental setup and post-processing can be found in Manohar *et al.* (2026). Figs. 1d,e show representative joint histograms of $(a^{(1)}, s^{(1)})$ and $(a^{(1)}, s^{(3)})$ from the 15 Hz PIV data. These histograms illustrate the characteristic parabolic envelopes. Most samples lie near the centreline-symmetric state $a^{(1)} \approx 0$, whereas large $|a^{(1)}|$ values, associated with strong spanwise wake excursions, coincide with large $|s^{(n)}|$.

2.2 Sensor-based Estimation for Upsampling

Since the wall-pressure data from the 14 sensors resolve both the LF and HF content of the wake, they are used as inputs to learn the map $\mathscr{F}_\theta : \mathbf{P}_k \mapsto \mathbf{y}_k$ from a multi-tap pressure window to instantaneous modal coefficients at time t_k, with $\mathbf{P}_k = \left[p_1(t_k - T_b{:}t_k + T_a), \ldots, p_{14}(t_k - T_b{:}t_k + T_a)\right]$ and $\mathbf{y}_k = \left[a^{(1)}(t_k), s^{(1)}(t_k), \ldots, s^{(m_s)}(t_k)\right]$.

We use T_b=2 s, T_a=0.1 s, and m_s=5. Pressure channels are low-pass filtered at approximately 270 Hz, resampled to f_s = 1.2 kHz, and normalized using a per-channel z-score. This limits the resolvable bandwidth to $\sim$270 Hz; resampling increases temporal resolution for learning but does not introduce additional physical frequency content. Only the leading antisymmetric coefficient $a^{(1)}$ is retained, as it captures the dominant VLF meandering mode ($\sim$1 Hz) and contains approximately 20% of the planar fluctuating energy (Manohar *et al.*, 2026). It is modeled together with the first five symmetric coefficients, which contain $\sim$10% of the energy and exhibit the strongest parabolic structure in their joint histograms with $a^{(1)}$. Higher-order antisymmetric coefficients lack coherent spectral signatures and are therefore excluded.

The network is a lightweight temporal Transformer encoder trained with mean-square-error on the coefficients. Specifically, the loss function minimizes the L_2 norm between the predicted coefficient vector $\widetilde{\mathbf{y}}$ and the ground truth PIV vector $\mathbf{y} = [a^{(1)}, s^{(1)}, \ldots, s^{(5)}]^\top$ exclusively at the sparse 15 Hz PIV timestamps t_i $\mathscr{L} = \frac{1}{N}\sum_{i=1}^{N} \|\widetilde{\mathbf{y}}(t_i) - \mathbf{y}(t_i)\|_2^2$, where N is the number of available PIV snapshots in a given training batch and superscript $\top$ is the matrix transpose. Inference uses a sliding window over the test sensor data to produce kHz-rate sequences $\{\widetilde{a}^{(1)}, \widetilde{s}^{(1-5)}\}$ at $f_s = 1.2$ kHz. The architecture is fundamentally similar to the one used by Manohar *et al.* (2023), except here we use a Transformer instead of a long short-term memory network. Additional details about the architecture and hyperparameters are in Appendix A.2.

2.3 Coefficient-Based Spectral POD

While spatial POD efficiently isolates the dominant energetic structures of the wake, its modal coefficients generally remain spectrally mixed. Since Hilbert-based envelope extraction requires a narrowband signal, the LF and HF motions must first be separated within the reduced coefficient space.

To achieve this separation, we employ Spectral Proper Orthogonal Decomposition (SPOD) (Towne *et al.*, 2018) on the upsampled symmetric coefficient vector. Because the temporal-Transformer predictions are restricted to a truncated basis of $m_s = 5$ spatial POD modes, the reconstructed symmetric velocity field may be written as $\hat{\mathbf{u}}_S(\mathbf{x}, f) = \mathbf{\Phi}_S(\mathbf{x})\hat{\mathbf{q}}_S(f)$, where $\mathbf{\Phi}_S(\mathbf{x}) \in \mathbb{R}^{M\times m_s}$ contains the retained symmetric spatial POD modes and $\hat{\mathbf{q}}_S(f) \in \mathbb{C}^{m_s}$ denotes the Fourier-transformed modal coefficients. The SPOD cross-spectral density tensor of the reconstructed symmetric field is defined as $\mathbf{S}^S_{uu}(\mathbf{x}, \mathbf{x}', f) = \mathbb{E}\left[\hat{\mathbf{u}}_S(\mathbf{x}, f)\hat{\mathbf{u}}_S^H(\mathbf{x}', f)\right]$, where the superscript H is the Hermitian transpose. Substituting the POD expansion of $\hat{\mathbf{u}}_S(\mathbf{x}, f)$ and noting that $\mathbf{\Phi}_S$ is deterministic and independent of frequency,

$$\mathbf{S}^S_{uu}(\mathbf{x}, \mathbf{x}', f) = \mathbf{\Phi}_S(\mathbf{x})\mathbf{S}^S_{qq}(f)\mathbf{\Phi}_S^\top(\mathbf{x}'), \tag{2}$$

where $\mathbf{S}^S_{qq}(f) = \mathbb{E}[\hat{\mathbf{q}}_S(f)\hat{\mathbf{q}}_S^H(f)] \in \mathbb{C}^{m_s\times m_s}$ is the discretized cross-spectral density matrix of the retained symmetric coefficients.

Since the reconstructed symmetric field is restricted to the span of the retained POD basis $\mathbf{\Phi}_S(\mathbf{x})$, the associated discrete cross-spectral density operator from Eq. (2), $\mathbf{S}^S_{uu}(f) = \mathbf{\Phi}_S\mathbf{S}^S_{qq}(f)\mathbf{\Phi}_S^\top \in \mathbb{C}^{M\times M}$, also maps vectors back into that same subspace. Therefore, the range of $\mathbf{S}^S_{uu}(f)$ is contained in span($\mathbf{\Phi}_S$). Moreover, any eigenvector of $\mathbf{S}^S_{uu}(f)$—i.e., an SPOD mode, $\boldsymbol{\psi}_S^{(k)}(f) \in \mathbb{C}^M$—associated with a nonzero eigenvalue must lie in the range of $\mathbf{S}^S_{uu}(f)$ by definition, and hence must also lie within span($\mathbf{\Phi}_S$). This admits the ansatz:

$$\boldsymbol{\psi}_S^{(k)}(\mathbf{x}, f) = \mathbf{\Phi}_S(\mathbf{x})\mathbf{\Theta}^{(k)}(f), \tag{3}$$

where $\mathbf{\Theta}^{(k)}(f)$ is the kth coefficient-space symmetric SPOD mode, hereafter referred to as the C-SPOD weighting vector.

Using the orthonormality of the retained POD basis, $\mathbf{\Phi}_S^\top\mathbf{\Phi}_S = \mathbf{I}$, the full discrete SPOD eigenvalue problem for the reconstructed symmetric flow reduces to the coefficient-space problem

$$\mathbf{S}^S_{qq}(f)\mathbf{\Theta}^{(k)}(f) = \lambda^{(k)}_{qq}(f)\mathbf{\Theta}^{(k)}(f). \tag{4}$$

Thus, SPOD can be performed entirely within the reduced symmetric coefficient space while yielding the same spectral energies as full-field SPOD of the reconstructed symmetric flow component—see Appendix A.3 for the proof.

In practice, we extract the relevant C-SPOD weighting vectors at the two frequencies of interest: approximately 13.5 Hz for the LF breathing motion and 135 Hz for the HF shedding motion. The 13.5 Hz breathing signal is associated with C-SPOD Mode 2, whereas the 135 Hz shedding signal is associated with C-SPOD Mode 1, based on their dominant signatures in the premultiplied C-SPOD eigenvalue spectra in Fig. 3b. The corresponding complex weighting vectors are denoted as $\mathbf{\Theta}_{\mathrm{LF}} = \mathbf{\Theta}^{(2)}(13.5\text{ Hz})$ and $\mathbf{\Theta}_{\mathrm{HF}} = \mathbf{\Theta}^{(1)}(135\text{ Hz})$.

2.4 Amplitude-Modulation Diagnostics

To test the AM hypothesis, we first isolate the slow VLF meandering mode that acts as the primary driver. A zero-phase band-pass filter is applied to the upsampled leading antisymmetric coefficient to isolate the VLF band, $a_{\mathrm{VLF}}(t) = \mathscr{B}_{\mathrm{VLF}}\{\widetilde{a}^{(1)}(t)\}$, where $\mathscr{B}_{\mathrm{VLF}}$ denotes a zero-phase band-pass filter over 0.5–3 Hz (see Table 1). The corresponding analytic signal is then constructed as $z_a(t) = a_{\mathrm{VLF}}(t) + i\mathscr{H}\{a_{\mathrm{VLF}}(t)\}$, where $\mathscr{H}$ is the Hilbert transform, from which we extract both the instantaneous VLF driver amplitude $A(t) = |z_a(t)|$ and phase $\Phi(t) = \arg z_a(t)$.

Next, we isolate the symmetric LF and HF responses. Let $\widetilde{\mathbf{y}}_S(t) = [\widetilde{s}^{(1)}(t), \ldots, \widetilde{s}^{(5)}(t)]^\top$ denote the upsampled symmetric POD coefficient vector. Using the (complex-valued) C-SPOD weighting vectors extracted at 13.5 Hz and 135 Hz, we form the corresponding (real-valued) 1D projected signals $s_{\mathrm{LF,raw}}(t) = \Re\left[\widetilde{\mathbf{y}}_S^\top(t)\mathbf{\Theta}_{\mathrm{LF}}\right]$, and $s_{\mathrm{HF,raw}}(t) = \Re\left[\widetilde{\mathbf{y}}_S^\top(t)\mathbf{\Theta}_{\mathrm{HF}}\right]$.

These projected signals are then band-pass filtered to isolate the breathing and shedding bands: $s_{\mathrm{LF}}(t) = \mathscr{B}_{\mathrm{LF}}\{s_{\mathrm{LF,raw}}(t)\}$, and $s_{\mathrm{HF}}(t) = \mathscr{B}_{\mathrm{HF}}\{s_{\mathrm{HF,raw}}(t)\}$, where $\mathscr{B}_{\mathrm{LF}}$ and $\mathscr{B}_{\mathrm{HF}}$ denote zero-phase band-pass filters. The band-limited ranges are chosen based on the frequency ranges spanned by each of these motions as observed in the premultiplied power spectral densities (PSD) of the modal coefficients in Fig. 3—summarized in Table 1.

Table 1. Zero-phase band-pass filter notation, frequency ranges, and associated target motions and signals.

Filter	Freq. Range	Target Motion	Target Signal
$\mathscr{B}_{\mathrm{VLF}}$	0.5–3 Hz	VLF meander	$\widetilde{a}^{(1)}(t)$
$\mathscr{B}_{\mathrm{LF}}$	0.5–20 Hz	LF breathing	$\Re[\widetilde{\mathbf{y}}_S^\top(t)\mathbf{\Theta}_{\mathrm{LF}}]$
$\mathscr{B}_{\mathrm{HF}}$	30–200 Hz	HF shedding	$\Re[\widetilde{\mathbf{y}}_S^\top(t)\mathbf{\Theta}_{\mathrm{HF}}]$

We then compute the analytic amplitude envelopes of these band-limited signals using the Hilbert transform and standardize them into the z-scored metric $Z^{\mathscr{B}}(t) = \left(\left|s_{\mathscr{B}}(t) + i\mathscr{H}\{s_{\mathscr{B}}(t)\}\right| - \mu_{\mathscr{B}}\right)/\sigma_{\mathscr{B}}$, where $\mu_{\mathscr{B}}$ and $\sigma_{\mathscr{B}}$ denote the temporal mean and standard deviation of the corresponding raw analytic envelope for $\mathscr{B} \in \{\mathrm{LF}, \mathrm{HF}\}$. Positive values indicate that the motion is amplified relative to its temporal baseline, whereas negative values indicate suppression. The narrowband assumption of the Hilbert transform is enforced by combining C-SPOD-based subspace separation with band-pass filtering. In practice, we study the quantity $\overline{Z}^{\mathscr{B}}(c_j) = \mathbb{E}_t\left[Z^{\mathscr{B}}(t)\,\middle|\,A(t) \in c_j\right]$, which denotes the envelope conditioned on the VLF amplitude $A(t)$, where we restrict the amplitude domain to the 1st through 99th percentiles of $A(t)$ and partition this range into equal-width amplitude bins c_j to reduce the influence of extreme outliers.

Finally, to examine how the LF and HF envelope levels vary with both the instantaneous VLF amplitude and phase, we bin the meander phase $\Phi(t)$ into $K = 8$ equal-width angular bins ϕ_k spanning $[-\pi, \pi]$. The phase-conditioned mean envelope is then defined as

$$\overline{Z}_k^{\mathscr{B}}(c_j) = \mathbb{E}_t\left[Z^{\mathscr{B}}(t)\,\middle|\,\Phi(t) \in \phi_k,\, A(t) \in c_j\right], \qquad (5)$$

where $\mathscr{B} \in \{\mathrm{LF}, \mathrm{HF}\}$. An increasing trend of $\overline{Z}^{\mathscr{B}}$ with respect to A signifies strengthening of the motion in band $\mathscr{B}$, whereas a decreasing trend signifies weakening.

3 RESULTS & DISCUSSION

3.1 Upsampling Validation and the Parabola

To assess whether the learned upsampling map generalizes to unseen data, phase-portrait analyses are performed on the unseen test record ($\sim$28 s). As shown in Fig. 2a, phase portraits of $(\widetilde{a}^{(1)}, \widetilde{s}^{(1)})$ built from the upsampled test coefficients reproduce the characteristic parabolic envelope observed in the low-rate 15 Hz ground truth measurements.

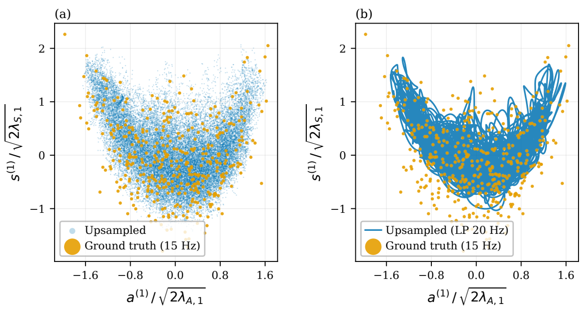

Figure 2. Upsampling on test data. (a) Phase portrait of unfiltered upsampled coefficients $(\widetilde{a}^{(1)}, \widetilde{s}^{(1)})$ with 15 Hz ground truth. (b) Low-pass filtered (< 20 Hz) upsampled coefficients.

To isolate the LF breathing contribution at 13.5 Hz, the upsampled $\widetilde{s}^{(1)}$ is low-pass filtered to < 20 Hz (Fig. 2b). The parabolic envelope persists, which suggests that the LF breathing contribution accounts for most of the parabolic structure, while the HF contribution appears mainly as higher-frequency fluctuations about the underlying LF manifold. Resolving these low-frequency trajectories demonstrates that the upsampled coefficients retain the relevant dynamical structure required for subsequent envelope extraction.

3.2 SPOD Mode Isolation & Demodulation

Before envelope extraction, the LF breathing and HF shedding contributions must first be spectrally separated. Fig. 3 presents both the spectral validation of the temporal upsampling and the subsequent LF/HF subspace separation via C-SPOD. We report premultiplied spectra from the training set because the short unseen test record contains too few realizations of the 1 Hz VLF cycle to cleanly resolve that peak.

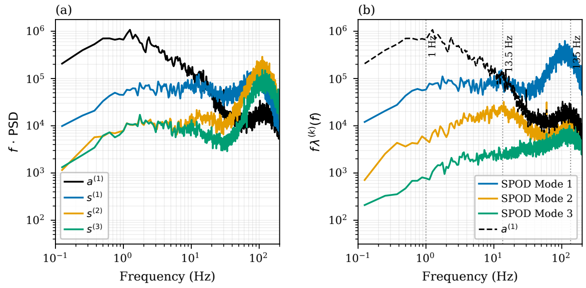

Figure 3. (a) Premultiplied PSDs of upsampled POD coefficients. (b) Premultiplied C-SPOD eigenvalue spectra computed on symmetric subspace, with $\widetilde{a}^{(1)}$ spectra for reference.

The premultiplied PSDs in Fig. 3a show that the temporal Transformer successfully recovers the VLF peak ($\sim$1 Hz) in $a^{(1)}$, alongside the broadband LF breathing ($\sim$13.5 Hz) and HF shedding ($\sim$135 Hz) humps that remain spectrally mixed across the symmetric POD coefficients. Applying C-SPOD to the symmetric coefficient vector (Fig. 3b) yields a much cleaner spectral separation. SPOD Mode 1 cleanly isolates the 135 Hz shedding band, while SPOD Mode 2 isolates the 13.5 Hz breathing band. These modes define the coefficient-space weighting vectors $\mathbf{\Theta}_{\mathrm{LF}}$ and $\mathbf{\Theta}_{\mathrm{HF}}$ associated with the LF breathing and HF shedding motions, respectively.

Fig. 4 illustrates this demodulation procedure. The top panel shows the slow driver signal $a_{\mathrm{VLF}}(t) = \mathscr{B}_{\mathrm{VLF}}\{\widetilde{a}^{(1)}(t)\}$ together with its analytic envelope $A(t) = |z_a(t)|$. The bottom panel shows the LF breathing carrier signal $s_{\mathrm{LF}}(t) = \mathscr{B}_{\mathrm{LF}}\{\Re[\widetilde{\mathbf{y}}_S^\top(t)\mathbf{\Theta}_{\mathrm{LF}}]\}$ with its analytic envelope $|s_{\mathrm{LF}}(t) + i\mathscr{H}\{s_{\mathrm{LF}}(t)\}|$. Periods of large LF carrier amplitude tend to coincide with large values of the VLF envelope, suggesting AM between the slow antisymmetric meander and the faster symmetric breathing motion.

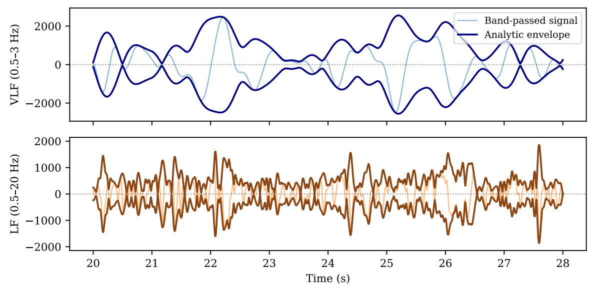

Figure 4. Top: band-pass filtered VLF meander signal $a_{\mathrm{VLF}}(t)$ and its analytic envelope $A(t)$. Bottom: LF breathing carrier signal $s_{\mathrm{LF}}(t)$ and its analytic envelope. Lower envelope mirrored about zero for visualization only.

3.3 Frequency-Dependent AM

Fig. 5 shows the VLF-amplitude-conditioned z-scored envelopes $\overline{Z}^{\mathrm{LF/HF}}$ of the SPOD-isolated bands as a function of the normalized VLF driver amplitude $A(t)$. The LF breathing and HF shedding bands exhibit fundamentally different trends. The LF breathing band exhibits a monotonic strengthening

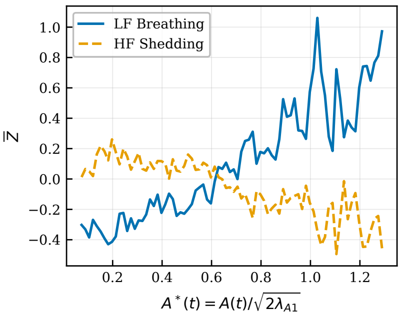

Figure 5. Conditionally averaged z-scored analytic envelopes $Z^{\mathrm{LF/HF}}$ as function of normalized VLF amplitude $A(t)$.

trend with increasing meander amplitude. Reflection symmetry implies that the leading-order forcing from the antisymmetric VLF mode into the symmetric subspace is quadratic in $a^{(1)}$. However, because the measured AM curves represent conditional averages over many internal wake states, they need not follow a purely quadratic dependence. The strong upward trend in the LF envelope therefore suggests that the LF breathing motion is the primary symmetric response associated with the VLF meander. Conversely, the HF shedding band exhibits a steady weakening with increasing meander amplitude. This indicates that strong spanwise wake excursions are associated with enhanced LF breathing activity but diminished HF shedding. Together, the observed LF strengthening and HF weakening suggest that strong meander states redistribute energy away from the HF shedding band and toward the LF breathing band.

3.4 Phase-Conditioned AM & Extreme Events

To further examine the inter-modal interaction, we phase-condition the mean envelopes $\overline{Z}_k^{\mathscr{B}}(c_j)$ using the instantaneous phase of the VLF meander, $\Phi(t)$, where the subscript k indexes the discrete VLF meander phase bin $\phi_k \in [-\pi, \pi]$. As shown in Fig. 6, conditioning on the meander phase reveals a second layer of organization. At low to moderate VLF amplitudes, the LF envelope curves remain relatively tightly clustered. However, at strong meander amplitudes ($A/\sqrt{2\lambda_{A1}} \geq 1$,

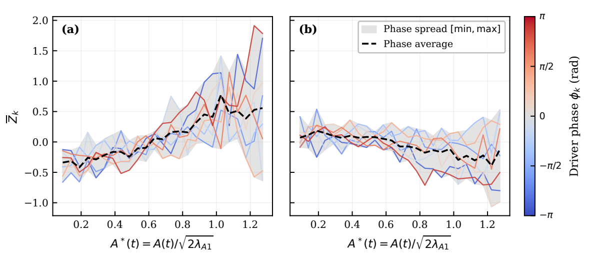

Figure 6. Phase-conditioned mean analytic envelopes for the (a) LF and (b) HF bands. Warm and cool colors correspond to opposite phases of the VLF cycle. Gray shaded region indicates pointwise phase spread. Dashed black curve is phase-averaged mean.

where λ_{A1} is the eigenvalue associated with $a^{(1)}$), the phase curves diverge substantially. This indicates that the strongest amplification of the LF breathing mode occurs preferentially at specific phases of the meander cycle, rather than uniformly across all strong meander events. The HF shedding band also becomes phase-dependent at large meander amplitudes, with the strongest suppression localized to particular phases.

To quantify this phase organization more directly, we isolate extreme meander events by selecting times for which the VLF amplitude $A(t)$ exceeds its 95th percentile. We then compare the phase-conditioned mean envelopes during these extreme events, $\overline{Z}_k^{\mathrm{ext}}$, against the corresponding phase-conditioned mean across all amplitudes, $\overline{Z}_k^{\mathrm{all}}$. The Δ_k curve $\Delta_k = \overline{Z}_k^{\mathrm{ext}} - \overline{Z}_k^{\mathrm{all}}$ measures the excess response conditioned on phase bin ϕ_k. Positive values indicate excess strengthening during extreme meander events, whereas negative values indicate excess weakening. To account for serial dependence, 95% confidence bands are estimated using a non-overlapping block bootstrap with 2-second blocks and 500 resamples.

Fig. 7 shows that the LF and HF bands exhibit complementary phase-dependent responses during extreme meander events. Near the phases associated with the largest wake

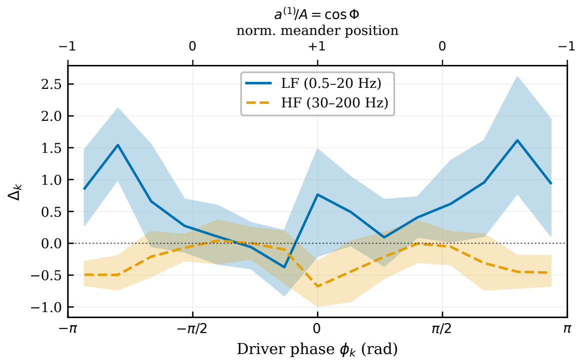

Figure 7. Phase-conditioned extreme-event curves isolating excess response during extreme VLF meander events ($A(t)$ above 95th percentile). Shaded regions denote 95% confidence intervals. Top axis indicates normalized instantaneous meander position, $a^{(1)}/A = \cos\Phi$. Unconditional mean level at $\Delta_k = 0$ (horizontal dashed line).

deflections ($\Phi = \{0, \pm\pi\}$), the LF breathing band reaches its greatest excess amplification while the HF shedding band reaches its greatest suppression. As the wake returns toward the centreline ($\Phi = \pm\pi/2$), both responses relax toward their unconditional mean levels. Thus, the strongest redistribution of energy between the LF and HF bands occurs near the phases of maximum spanwise wake displacement.

4 CONCLUSIONS

The present results show that the nonlinear interactions between unsteady modes with disparate timescales can manifest as amplitude modulation (AM) between symmetric and antisymmetric wake dynamics. In particular, this study examines the parabolic envelopes observed in the low-probability rims of the joint histograms between the dominant antisymmetric and symmetric proper orthogonal decomposition (POD) coefficients in the wake of a 3D Gaussian bump. By training a temporal Transformer to upsample 15 Hz PIV into time-resolved sequences, we recover spectral content consistent with that observed in the wall-pressure signals: a very-low-frequency (VLF) spanwise meander near 1 Hz, the broadband low-frequency (LF) breathing motion near 13.5 Hz, and the broadband high-frequency (HF) centreline shedding near 135 Hz. By spectrally isolating the symmetric bands and examining their low-pass-filtered (< 20 Hz) phase portraits, we find that the characteristic parabolic structure is retained, suggesting that the parabola is primarily associated with the LF breathing dynamics rather than the HF shedding motion. Furthermore, by extracting the amplitude envelopes of the symmetric bands, we observe a distinct, frequency-dependent AM response associated with extreme VLF spanwise excursions. Specifically, the data show that as the meander amplitude increases, the LF breathing mode envelope strengthens whereas the HF shedding envelope weakens. Both the LF strengthening and HF weakening also appear to be phase-organized with respect to the extreme states of the VLF meander cycle. The observed LF strengthening and HF weakening are therefore consistent with a slow modulation of the wake state by the VLF meander, although distinguishing between additive forcing, parametric modulation, or other nonlinear interaction pathways remains an important target for future work.

ACKNOWLEDGMENTS

We would like to acknowledge the Natural Sciences and Engineering Research Council of Canada, Boeing Commercial Aircraft and their Flight Sciences Function Excellence group.

REFERENCES

Da Silva, Barbara L, Sumner, David & Bergstrom, Donald J 2024 On the flow dynamics around a surface-mounted cube and boundary layer effects. *Journal of Fluid Mechanics* **991**, A17.

Holmes, Philip 2012 *Turbulence, coherent structures, dynamical systems and symmetry*. Cambridge university press.

Manohar, K.H., Williams, O., Martinuzzi, R.J. & Morton, C. 2023 Temporal super-resolution using smart sensors for turbulent separated flows. *Experiments in Fluids* **64** (5), 101.

Manohar, Kevin H, Annamalai, Hariprasad, Williams, Owen, Morton, Chris & Martinuzzi, Robert J 2026 Unsteadiness in turbulent separated flow over a three-dimensional Gaussian bump. *arXiv preprint arXiv:2603.05765* .

Noack, Bernd R, Afanasiev, Konstantin, Morzyński, Marek, Tadmor, Gilead & Thiele, Frank 2003 A hierarchy of low-dimensional models for the transient and post-transient cylinder wake. *Journal of Fluid Mechanics* **497**, 335–363.

Towne, Aaron, Schmidt, Oliver T & Colonius, Tim 2018 Spectral proper orthogonal decomposition and its relationship to dynamic mode decomposition and resolvent analysis. *Journal of Fluid Mechanics* **847**, 821–867.

Vaswani, Ashish, Shazeer, Noam, Parmar, Niki, Uszkoreit, Jakob, Jones, Llion, Gomez, Aidan N, Kaiser, Łukasz & Polosukhin, Illia 2017 Attention is all you need. *Advances in Neural Information Processing Systems* **30**.

Williams, O., Samuell, M. & Sarwas, E.S. et al. 2020 Experimental study of a cfd validation test case for turbulent separated flows. In *AIAA Scitech 2020 Forum*, p. 0092.

A APPENDIX

A.1 Quadratic Mode Coupling

Defining the reflection operator as $\mathscr{R} : (x,y,z) \mapsto (x,-y,z)$, the S/A POD basis inherits definite symmetry under $\mathscr{R}$: antisymmetric modes satisfy $\mathscr{R}\Phi_A = -\Phi_A$, and symmetric modes satisfy $\mathscr{R}\Phi_S = +\Phi_S$ (Holmes, 2012). In a Galerkin projection of the nonlinear convective term, the triadic interaction coefficients take the form: $q_{ijk} = \int_\Omega \Phi_i \cdot (\Phi_j \cdot \nabla)\Phi_k \, d\Omega$. Because the integration domain Ω is reflection-symmetric, any integrand that is odd under $\mathscr{R}$ integrates to zero. Let $par(\cdot) \in \{\pm 1\}$ be a parity label for S/A modes such that $par(S) = +1$ and $par(A) = -1$, respectively. The parity of the integrand is $par(\Phi_i)\, par(\Phi_j)\, par(\Phi_k)$, which is non-zero only for select quadratic couplings: $A \times A \to S$, $A \times S \to A$, and $S \times S \to S$. Consequently, the leading-order forcing from $a^{(1)}$ into the symmetric subspace must arise through its quadratic self-interaction. Projecting the Navier-Stokes equations onto $\Phi_{S,n}$ yields $\dot{s}^{(n)} \approx \lambda_{S,n} s^{(n)} + \gamma_n [a^{(1)}]^2 + \ldots$, where $\lambda_{S,n}$ is the linear growth or decay rate of $\Phi_{S,n}$ and γ_n is the corresponding quadratic coupling associated with the self-interaction of $a^{(1)}$, and the omitted terms represent higher-order symmetric–symmetric and mixed interactions.

A.2 Temporal Transformer Architecture

The chosen upsampler is a temporal Transformer encoder that maps a 14-channel pressure window to the instantaneous POD modal coefficients. The synchronized pressure–PIV samples were divided into 70%/15%/15% train/validation/test subsets.
Input and Embedding. The model receives a z-score normalized pressure tensor $\mathbf{X} \in \mathbb{R}^{B\times 14\times L}$, where B is the batch size (32). The temporal window $L = 2521$ comprises a look-back interval of $T_b = 2.0\,\mathrm{s}$ and a look-ahead interval of $T_a = 0.1\,\mathrm{s}$ sampled at $f_s = 1.2\,\mathrm{kHz}$. A point-wise convolution projects the 14 sensor channels to model dimension of $d = 64$, followed by fixed sinusoidal positional encodings (Vaswani *et al.*, 2017).
Transformer Trunk and Output. The sequence is processed by $N_\ell = 4$ identical Pre-LN Transformer encoder layers. Each layer applies multi-head self-attention ($h = 4$ heads with dimension 16), a position-wise feed-forward network (hidden size 256) with GELU activations, and dropout of $p = 0.2$. Following the encoder trunk, the final temporal token is extracted and passed through a single linear projection to output the $m_s = 5$ symmetric and leading antisymmetric coefficients.
Training Protocol. Optimization is performed using AdamW with a base learning rate of 10^{-3} and a weight decay of 10^{-4}. The learning rate is decayed following a cosine annealing schedule. Models are trained for a maximum of 100 epochs, utilizing early stopping to prevent overfitting.

A.3 Eigenvalue Equivalence of C-SPOD

Consider the discrete SPOD eigenvalue problem for the reconstructed symmetric field,

$$\mathbf{S}^S_{uu}(f)\boldsymbol{\psi}^{(k)}_S(f) = \lambda^{(k)}_{uu}(f)\boldsymbol{\psi}^{(k)}_S(f). \tag{6}$$

Substituting Eqs. (2) and (3) into the LHS of Eq. (6):

$$\begin{aligned}
\mathbf{S}^S_{uu}(f)\boldsymbol{\psi}^{(k)}_S(f) &= \left(\mathbf{\Phi}_S\mathbf{S}^S_{qq}(f)\mathbf{\Phi}_S^\top\right)\left(\mathbf{\Phi}_S\mathbf{\Theta}^{(k)}(f)\right) \\
&= \mathbf{\Phi}_S\mathbf{S}^S_{qq}(f)\mathbf{\Theta}^{(k)}(f) \qquad (\text{since } \mathbf{\Phi}_S^\top\mathbf{\Phi}_S = \mathbf{I}) \\
&= \mathbf{\Phi}_S\lambda^{(k)}_{qq}(f)\mathbf{\Theta}^{(k)}(f) \qquad (\text{by Eq. (4)}) \\
&= \lambda^{(k)}_{qq}(f)\boldsymbol{\psi}^{(k)}_S(f) \qquad (\text{by Eq. (3)}) \\
&= \lambda^{(k)}_{uu}(f)\boldsymbol{\psi}^{(k)}_S(f) \qquad (\text{by Eq. (6)})
\end{aligned}$$

Thus, $\lambda^{(k)}_{uu}(f) = \lambda^{(k)}_{qq}(f)$, concluding the proof.